

---

# Galaxy Clusters in the Radio: Relativistic Plasma and ICM/Radio Galaxy Interaction Processes

Luigina Feretti<sup>1</sup> and Gabriele Giovannini<sup>1,2</sup>

<sup>1</sup>Istituto di Radioastronomia INAF, Via P. Gobetti 101, 40129 Bologna (Italy)  
lferetti@ira.inaf.it

<sup>2</sup>Dipartimento di Astronomia, Università di Bologna, Via Ranzani 1, 40127 Bologna (Italy)  
gabriele.giovannini@unibo.it

## 1 Introduction

Studies at radio wavelengths allow the investigation of important components of clusters of galaxies. The most spectacular aspect of cluster radio emission is represented by the large-scale diffuse radio sources, which cannot be obviously associated with any individual galaxy. These sources indicate the existence of relativistic particles and magnetic fields in the cluster volume, thus the presence of non-thermal processes in the hot intracluster medium (ICM). The knowledge of the properties of these sources has increased significantly in recent years, due to higher sensitivity radio images and to the development of theoretical models. The importance of these sources is that they are large scale features, which are related to other cluster properties in the optical and X-ray domain, and are thus directly connected to the cluster history and evolution.

The radio emission in clusters can also originate from individual galaxies, which have been imaged over the last decades with sensitive radio telescopes. The emission from radio galaxies often extends well beyond their optical boundaries, out to hundreds of kiloparsec, and hence it is expected that the ICM would affect their structure. This interaction is indeed observed in extreme examples: the existence of radio galaxies showing distorted structures (tailed radio sources), and radio sources filling X-ray cavities at the centre of cooling core clusters. Finally, the cluster environment may play a role in the statistical radio properties of galaxies, i.e. their probability of forming radio sources.

The organization of this paper is as follows: The basic formulae used to derive the age of synchrotron sources and the equipartition parameters are presented in § 2, while the observational properties of diffuse radio sources are presented in § 3. Then in § 4 we give a general outline of the models of

the relativistic particle origin and re-acceleration; while the current results on cluster magnetic fields are described in § 5. Finally, § 6 reports the properties of cluster radio emitting galaxies.

The intrinsic parameters quoted in this paper are computed for a  $\Lambda$ CDM cosmology with  $H_0 = 70 \text{ km s}^{-1}\text{Mpc}^{-1}$ ,  $\Omega_m=0.3$ , and  $\Omega_\Lambda=0.7$ .

## 2 Basic formulas from the synchrotron theory

### 2.1 Synchrotron radiation

The synchrotron emission is produced by the spiralling motion of relativistic electrons in a magnetic field. An electron with energy  $E=\gamma m_e c^2$  (where  $\gamma$  is the Lorentz factor) in a magnetic field  $\mathbf{B}$ , experiences a  $\mathbf{v} \times \mathbf{B}$  force that causes it to follow a helical path along the field lines, emitting radiation into a cone of half-angle  $\simeq \gamma^{-1}$  about its instantaneous velocity. To the observer, the radiation is essentially a continuum with a fairly peaked spectrum concentrated near the frequency

$$\nu_{syn} = \frac{3e}{4\pi m_e^3 c^5} (B \sin \theta) e^2, \quad (1)$$

where  $\theta$  is the pitch angle between the electron velocity and the magnetic field direction. The synchrotron power emitted by a relativistic electron is

$$-\frac{dE}{dt} = \frac{2e^4}{3m_e^4 c^7} (B \sin \theta)^2 E^2. \quad (2)$$

In c.g.s units:

$$\begin{aligned} \nu_{syn} &\simeq 6.27 \times 10^{18} (B \sin \theta) E^2 \\ &\simeq 4.2 \times 10^6 (B \sin \theta) \gamma^2, \end{aligned} \quad (3)$$

$$\begin{aligned} -\frac{dE}{dt} &\simeq 2.37 \times 10^{-3} (B \sin \theta)^2 E^2 \\ &\simeq 1.6 \times 10^{-15} (B \sin \theta)^2 \gamma^2. \end{aligned} \quad (4)$$

From eqn. 3, it is easily derived that electrons of  $\gamma \simeq 10^3 - 10^4$  in magnetic fields of  $B \simeq 1 \mu \text{ G}$  radiate in the radio domain.

The case of astrophysical interest is that of a homogeneous and isotropic population of electrons with a power-law energy distribution, i.e., with the particle density between  $E$  and  $E+dE$  given by:

$$N(E)dE = N_0 E^{-\delta} dE. \quad (5)$$

To obtain the total monochromatic emissivity  $J(\nu)$ , one must integrate over the contributions of all electrons. In regions which are optically thin to their

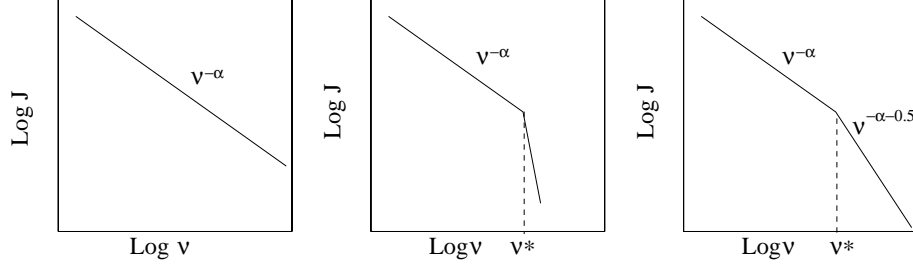


**Fig. 1.** Sketch of synchrotron spectra. The left panel shows a standard spectrum, the central panel shows an aged spectrum produced in a source with a single event of particle production, the right panel shows an aged spectrum with particle injection. The critical frequency  $\nu^*$  is related to the particle lifetime.

own radiation (i.e. without any internal absorption), the total intensity spectrum varies as [14]:

$$J(\nu) \propto N_0 (B \sin \theta)^{1+\alpha} \nu^{-\alpha}, \quad (6)$$

therefore it follows a power-law with spectral index related to the index of the electron energy distribution  $\alpha = (\delta - 1)/2$ .

## 2.2 Time evolution of the synchrotron spectrum

By integrating the expression of the electron energy loss (eqn. 2) it is found that the particle energy decreases with time, as:

$$E = \frac{E_0}{1 + b(B \sin \theta)^2 E_0 t}, \quad (7)$$

where  $E_0$  is the initial energy at  $t = 0$ , and  $b = 2e^4/(3m_e^4 c^7) = 2.37 \times 10^{-3}$  c.g.s units (see eqn. 4). Therefore, the particle energy halves after a time  $t^* = [b(B \sin \theta)^2 E_0]^{-1}$ . This is a characteristic time which can be identified as the particle lifetime. Similarly, we can define a characteristic energy  $E^* = [b(B \sin \theta)^2 t]^{-1}$ , such that a particle with energy  $E_0 > E^*$  will lose most of its energy in a time  $t^*$ .

In an ensemble of particles, the energy losses of each particle affect the overall particle energy distribution, and consequently the resulting synchrotron spectrum undergoes a modification. Indeed, after a time  $t^*$  the particles with  $E > E^*$  will lose most of their energy. This produces a critical frequency  $\nu^*$  in the radio spectrum, such that for  $\nu < \nu^*$  the spectrum is unchanged, whereas for  $\nu > \nu^*$  the spectrum steepens. If particles were produced in a single event with power law energy distribution,  $N(E, 0)dE = N_0 E^{-\delta} dE$ , the radio spectrum would fall rapidly to zero for  $\nu > \nu^*$ . In the case that new particles were injected in the source, the spectrum beyond  $\nu^*$  steepens by 0.5. These various cases are illustrated in Fig. 1. Any radio spectrum showing a cutoff is evidence

of ageing of the radio emitting particles. In addition, any spectrum showing no cutoff but having a steep spectral index is also indicative of ageing, since it naturally refers to a range of frequencies higher than the critical frequency. For a rigorous treatment of the evolution of synchrotron spectra we refer to [75] and [117].

From the critical frequency  $\nu^*$ , it is possible to derive the radiating electron lifetime, which represents the time since the particle production (or the time since the last injection event, depending on the shape of spectral steepening). Since the synchrotron emission depends on  $\sin \theta$  (eqn. 1), one has to take into account the distribution of electron pitch angles. Moreover, for a correct evaluation, also the electron energy losses, due to the inverse Compton process, must be considered.

The electron lifetime (in Myr), assuming an *anisotropic* pitch angle distribution is given by:

$$t^* = 1060 \frac{B^{0.5}}{B^2 + \frac{2}{3}B_{\text{CMB}}^2} [(1+z)\nu^*]^{-0.5}, \quad (8)$$

where the magnetic field  $B$  is in  $\mu\text{G}$ , the frequency  $\nu$  is in GHz and  $B_{\text{CMB}} (= 3.25 (1+z)^2 \mu\text{G})$  is the equivalent magnetic field of the Cosmic Microwave Background. If the distribution of electron pitch angles is *isotropic*, the above formula becomes:

$$t^* = 1590 \frac{B^{0.5}}{B^2 + B_{\text{CMB}}^2} [(1+z)\nu^*]^{-0.5}. \quad (9)$$

A derivation of the expressions in eqs. 8 and 9 can be found in [111].

### 2.3 Energy content and equipartition magnetic fields

The total energy of a synchrotron source is due to the energy in relativistic particles ( $U_{el}$  in electrons and  $U_{pr}$  in protons) plus the energy in magnetic fields ( $U_B$ ):

$$U_{tot} = U_{el} + U_{pr} + U_B. \quad (10)$$

The magnetic field energy contained in the source volume  $V$  is given by

$$U_B = \frac{B^2}{8\pi} \Phi V, \quad (11)$$

where  $\Phi$  is the fraction of the source volume occupied by the magnetic field (filling factor). The electron total energy in the range  $E_1 - E_2$ ,

$$U_{el} = V \times \int_{E_1}^{E_2} N(E) E dE = V N_0 \int_{E_1}^{E_2} E^{-\delta+1} dE \quad (12)$$

can be expressed as a function of the synchrotron luminosity,  $L_{syn}$ , observed between two frequencies  $\nu_1$  and  $\nu_2$ , i.e.,

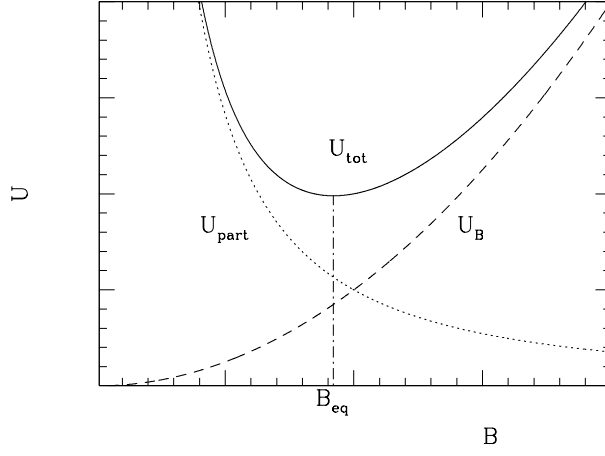


**Fig. 2.** Trend of the energy content in a radio source (in arbitrary units): the energy in magnetic fields is  $U_B \propto B^2$ , the energy in relativistic particles is  $U_{part} = U_{el} + U_{pr} \propto B^{-3/2}$ . The total energy content  $U_{tot}$  is minimum when the contributions of magnetic fields and relativistic particles are approximately equal (equipartition condition). The corresponding magnetic field is commonly referred to as equipartition value  $B_{eq}$ .

$$U_{el} = L_{syn}(B \sin \theta)^{-\frac{3}{2}} f(\delta, \nu_1, \nu_2), \quad (13)$$

where  $f(\delta, \nu_1, \nu_2)$  is a function of the index of the electron energy distribution and of the observing frequencies (see [96] for a rigorous derivation). The energy contained in the heavy particles,  $U_{pr}$ , can be related to  $U_{el}$  assuming:

$$U_{pr} = k U_{el}. \quad (14)$$

Finally, taking  $\sin \theta = 1$ , the total energy is:

$$U_{tot} = (1 + k) L_{syn} B^{-\frac{3}{2}} f(\delta, \nu_1, \nu_2) + \frac{B^2}{8\pi} \Phi V. \quad (15)$$

The trend of the radio source energy content is shown in Fig. 2. The condition of minimum energy,  $U_{min}$ , computed by equating to zero the first derivative of the expression of  $U_{tot}$  (eqn. 15), is obtained when the contributions of the magnetic field and the relativistic particles are approximately equal:

$$U_B = \frac{3}{4}(1 + k)U_{el}. \quad (16)$$

For this reason the minimum energy is known also as equipartition value.

The total minimum energy density  $u_{min} = U_{min}/V\Phi$ , assuming same volume in particles and magnetic field ( $\Phi=1$ ), and applying the K-correction, can be expressed in terms of observable parameters, as:

$$u_{\min} = 1.23 \times 10^{-12} (1+k)^{\frac{4}{7}} (\nu_0)^{\frac{4\alpha}{7}} (1+z)^{\frac{(12+4\alpha)}{7}} I_0^{\frac{4}{7}} d^{\frac{4}{7}}, \quad (17)$$

where  $I_0$  is the source brightness which is directly observed at the frequency  $\nu_0$ ,  $d$  is the source depth along the line of sight,  $z$  is the source redshift and  $\alpha$  is the spectral index of the radio emission. The energy density is in  $\text{erg cm}^{-3}$ ,  $\nu_0$  in MHz,  $I_0$  in  $\text{mJy arcsec}^{-2}$  and  $d$  in kpc.  $I_0$  can be measured from the contour levels of a radio image (for significantly extended sources) or can be obtained by dividing the source total flux by the source solid angle, while  $d$  can be inferred from geometrical arguments. The constant has been computed for  $\alpha = 0.7$ ,  $\nu_1 = 10$  MHz and  $\nu_2 = 100$  GHz (tabulated in [69], for other values of these parameters).

The magnetic field for which the total energy content is minimum is referred to as the equipartition value and is derived as follows:

$$B_{eq} = \left( \frac{24\pi}{7} u_{\min} \right)^{\frac{1}{2}}. \quad (18)$$

One must be aware of the uncertainties inherent to the determination of the minimum energy density and equipartition magnetic field strength. The value of  $k$ , the ratio of the energy in relativistic protons to that in electrons (eqn. 14), depends on the mechanism of generation of relativistic electrons, which, so far, is poorly known. Values usually assumed in literature for clusters are  $k = 1$  (or  $k = 0$ ). Uncertainties are also related to the volume filling factor  $\Phi$ .

In the standard approach presented above, the equipartition parameters are obtained from the synchrotron radio luminosity observed between the two fixed frequencies  $\nu_1$  and  $\nu_2$ . Brunetti et al. [18] demonstrated that it is more appropriate to calculate the radio source energy by integrating the synchrotron luminosity over a range of electron energies. This avoids the problem that electron energies corresponding to frequencies  $\nu_1$  and  $\nu_2$  depend on the magnetic field value (see eqn. 1), thus the integration over a range of fixed frequencies is equivalent to considering radiating electrons over a variable range of energies. Moreover, it has the advantage that electrons of very low energy are also taken into account. The equipartition quantities obtained by following this approach are presented by [18] and [6]. Representing the electron energy by its Lorentz factor  $\gamma$ , and assuming that  $\gamma_{\min} \ll \gamma_{\max}$ , the new expression for the equipartition magnetic field  $B'_{eq}$  in Gauss (for  $\alpha > 0.5$ ) is:

$$B'_{eq} \sim 1.1 \gamma_{\min}^{\frac{1-2\alpha}{3+\alpha}} B_{eq}^{\frac{7}{2(3+\alpha)}}, \quad (19)$$

where  $B_{eq}$  is the value of the equipartition magnetic field obtained with the standard formulae by integrating the radio spectrum between 10 MHz and 100 GHz. It should be noticed that  $B'_{eq}$  is larger than  $B_{eq}$  for  $B_{eq} < \gamma_{\min}^{-2}$  (see Fig. 3).

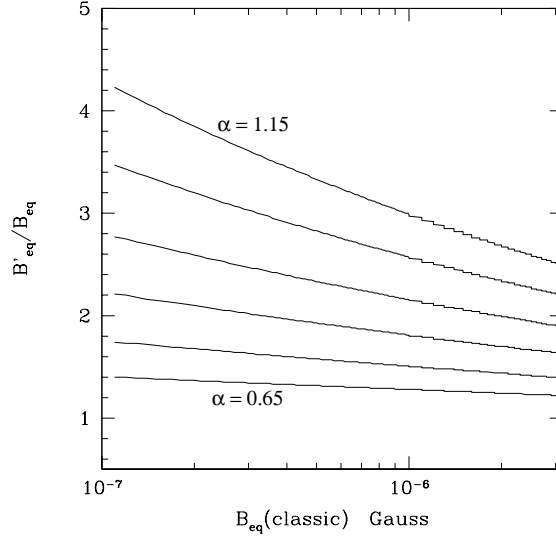


**Fig. 3.** Values of the ratio  $B'_{eq}/B_{eq}$  (see text) as a function of the equipartition magnetic field obtained with the classical approach, assuming an electron minimum Lorentz factor  $\gamma_{\min} = 50$ . Different lines refer to different values of the initial spectral index (i.e. not affected by ageing), from  $\alpha = 1.15$  (top line) to  $\alpha = 0.65$  (bottom line) in steps of  $\alpha = 0.1$ .

### 3 Radio emission from the ICM: diffuse radio sources

In recent years, there has been growing evidence for the existence of cluster large-scale diffuse radio sources, which have no optical counterpart and no obvious connection to cluster galaxies, and are therefore associated with the ICM. These sources are typically grouped in 3 classes: halos, relics and mini-halos. The number of clusters with halos and relics is presently around 50, and whose properties have been recently reviewed by Giovannini & Feretti [60] and Feretti [48]. The synchrotron nature of this radio emission indicates the presence of cluster-wide magnetic fields of the order of  $\sim 0.1\text{--}1\ \mu\text{G}$ , and of a population of relativistic electrons with Lorentz factor  $\gamma \gg 1000$ . The understanding of these non-thermal components is important for a comprehensive physical description of the ICM.

#### 3.1 Radio halos

Radio halos are diffuse radio sources of low surface brightness ( $\sim \mu\text{Jy arcsec}^{-2}$  at 20 cm) permeating the central volume of a cluster. They are typically extended with sizes  $\gtrsim 1\text{ Mpc}$  and are unpolarized down to a few percent level.

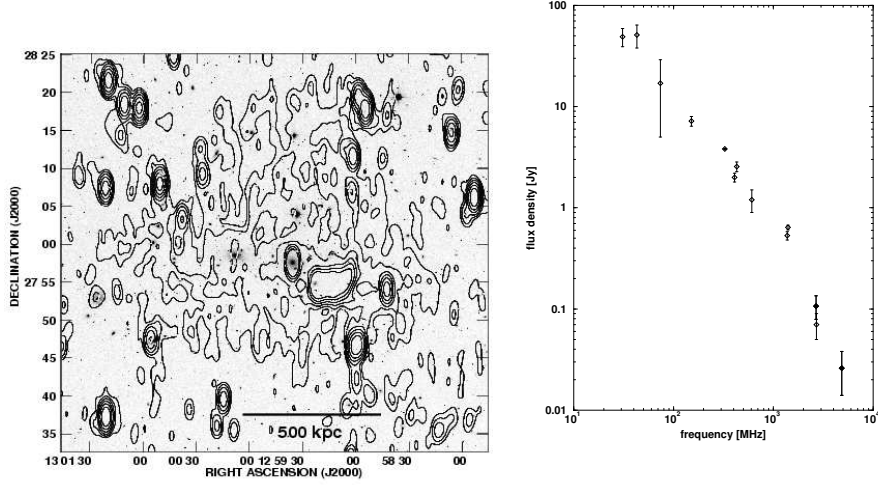


**Fig. 4.** **Left panel:** Diffuse radio halo Coma C in the Coma cluster ( $z = 0.023$ ) at 0.3 GHz, superimposed onto the optical image from the DSS1. The resolution of the radio image is  $55'' \times 125''$  (FWHM, RA  $\times$  DEC); contour levels are: 3, 6, 12, 25, 50, 100 mJy/beam. **Right panel:** Total radio spectrum of the radio halo Coma C (from [115]).

The prototype of this class is the diffuse source Coma C at the centre of the Coma cluster ([57] and Fig. 4), first classified by Willson [122]. The halo in A2163, shown in left panel of Fig. 5, is one of the most extended and powerful halos. Other well studied giant radio halos are present in A665 [59], A2219 [2], A2255 [42], A2319 [43], A2744 (Fig. 7, left panel), 1E0657-56 [84], and in the distant cluster CL 0016+16 [59] at redshift  $z = 0.555$ . All these clusters show recent merging processes, and no cooling core.

Radio halos of small size, i.e.  $\ll 1$  Mpc, have also been revealed in the central regions of clusters. Some examples are in A401 [59], A1300 [99], A2218 (Fig. 5, right panel) and A3562 [55]. All these clusters, as well as those hosting giant radio halos, are characterized by recent merger processes and no cooling core.

Unlike the presence of thermal X-ray emission, the presence of diffuse radio emission is not common in clusters of galaxies: the detection rate of radio halos, at the detection limit of the NRAO VLA Sky Survey (NVSS) is  $\sim 5\%$  in a complete cluster sample [58]. However, the probability is much larger, if clusters with high X-ray luminosity are considered. Indeed,  $\sim 35\%$  of clusters with X-ray luminosity larger than  $10^{45}$  erg s $^{-1}$  X-ray (in the ROSAT band 0.1-2.4 keV, computed assuming  $H_0 = 50$  km s $^{-1}$ Mpc $^{-1}$  and  $q_0 = 0.5$ ) show a giant radio halo [60].

The physical parameters in radio halos can be estimated assuming equipartition conditions, and further assuming equal energy in relativistic protons and



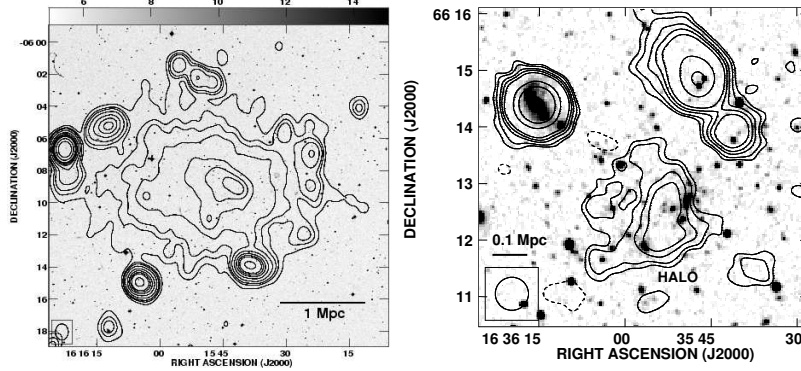


**Fig. 5. Left panel:** Radio emission in A2163 ( $z = 0.203$ ) at 20 cm [45]. The radio halo is one of the most powerful and extended halos known so far. **Right panel:** Radio emission of the cluster A2218 ( $z = 0.171$ ) at 20 cm [59]. In both clusters the radio contours are overlaid onto the grey-scale optical image.

electrons, a volume filling factor of 1, a low frequency cut-off of 10 MHz, and a high frequency cut-off of 10 GHz. The derived minimum energy densities in halos and relics are of the order of  $10^{-14} - 10^{-13} \text{ erg cm}^{-3}$ , i.e. much lower than the energy density in the thermal gas. The corresponding equipartition magnetic field strengths range from 0.1 to 1  $\mu\text{G}$ .

The total radio spectra of halos are steep ( $\alpha \gtrsim 1$ )<sup>1</sup>, as typically found in aged radio sources. Only a few halos have good multi-frequency observations that allow an accurate determination of their integrated spectrum. Among them, the spectrum of the Coma cluster halo is characterized by a steepening at high frequencies, which has been recently confirmed by single dish data (Fig. 4, right panel). The spectrum of the radio halo in A1914 is very steep, with an overall slope of  $\alpha \sim 1.8$ . A possible high frequency curvature is discussed by Komissarov & Gubanov [79]. In A754, Bacchi et al. [2] estimate  $\alpha_{0.3\text{GHz}}^{0.3\text{GHz}} \sim 1.1$ , and  $\alpha_{0.3\text{GHz}}^{1.4\text{GHz}} \sim 1.5$ , and infer the presence of a possible spectral cutoff. Indication of a high frequency spectral steepening is also obtained in the halo of A2319, where Feretti et al. [43] report  $\alpha_{0.4\text{GHz}}^{0.6\text{GHz}} \sim 0.9$  and  $\alpha_{0.6\text{GHz}}^{1.4\text{GHz}} \sim 2.2$ . In the few clusters where maps of the spectral index are available (Coma C, [57]; A665 and A2163, [49]), the radio spectrum steepens radially with the distance from the cluster centre. In addition, it is found that the spectrum in A665 and A2163 is flatter in the regions influenced by merger processes (see § 4.1).

In general, from the spectra of halos, it is derived that the radiative lifetime of the relativistic electrons, considering synchrotron and inverse Compton energy losses, is of the order of  $\sim 10^8 \text{ yr}$  [107]. Since the expected diffusion velocity of the electron population is of the order of the Alfvén speed ( $\sim 100 \text{ km s}^{-1}$ ), the radiative electron lifetime is too short to allow the particle diffu-

<sup>1</sup>  $S(\nu) \propto \nu^{-\alpha}$  as in eqn. 6

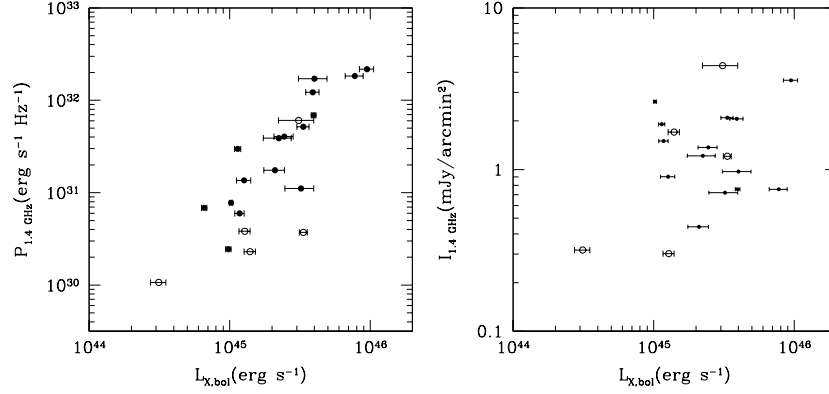


**Fig. 6. Left panel:** Monochromatic radio power at 20 cm versus cluster bolometric X-ray luminosity. **Right panel:** Average surface brightness of the radio halos versus cluster X-ray luminosity. In both panels, filled and open circles refer to halos of size  $>$  and  $<$  1 Mpc, respectively.

sion throughout the cluster volume. Thus, the radiating electrons cannot have been produced at some localized point of the cluster, but they must undergo *in situ* energization, acting with an efficiency comparable to the energy loss processes [97]. We will show in § 4 that recent cluster mergers are likely to supply energy to the halos and relics.

The radio and X-ray properties of halo clusters are related. The most powerful radio halos are detected in the clusters with the highest X-ray luminosity. This follows from the correlation shown in Fig. 6 between the monochromatic radio power of a halo at 20 cm and the bolometric X-ray luminosity of the parent cluster [84, 60]. The right panel of Fig. 6 shows the correlation between the average surface brightness of the radio halo and the cluster X-ray luminosity. Since the brightness is an observable, this correlation can be used to set upper limits to the radio emission to those clusters in which a radio halo is not detected. It is worth reminding the reader that the radio power versus X-ray luminosity correlation is valid for merging clusters with radio halos, and therefore cannot be generalized to all clusters. Among the clusters with high X-ray luminosity and no radio halo, there are A478, A576, A2204, A1795, A2029, all well known relaxed clusters with a massive cooling flow. An extrapolation of the above correlation to low radio and X-ray luminosities indicates that clusters with  $L_X \lesssim 10^{45} \text{ erg s}^{-1}$  would host halos of power of a few  $10^{23} \text{ W Hz}^{-1}$ . With a typical size of 1 Mpc, they would have a radio surface brightness (easily derived from the right panel of Fig. 6) lower than current limits obtained in the literature and in the NVSS. On the other hand, it is possible that giant halos are only present in the most X-ray luminous clusters, i.e. above a threshold of X-ray luminosity (see [2]). Future radio data with next generation instruments (LOFAR, LWA, SKA) will allow the detec-

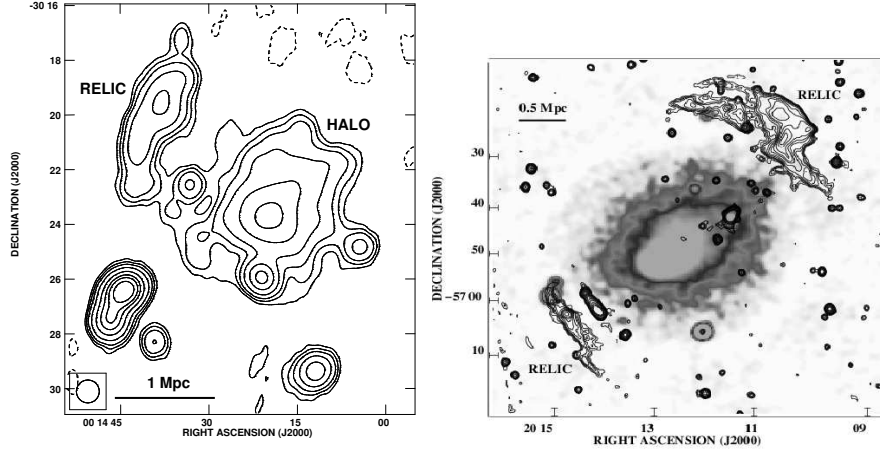


**Fig. 7. Left panel:** Radio emission of A2744 ( $z = 0.308$ ) showing a peripheral elongated relic, and a central radio halo [66]. **Right panel:** A3667 ( $z = 0.055$ ): contours of the radio emission at 36 cm [104] overlaid onto the grey-scale ROSAT X-ray image. Two radio relics are located on opposite sides of the cluster along the axis of the merger, with the individual radio structures elongated perpendicular to this axis.

tion of low brightness/low power large halos, in order to clarify if halos are present in all merging clusters or only in the most massive ones.

Since cluster X-ray luminosity and mass are correlated [100], the correlation between radio power ( $P_{1.4 \text{ GHz}}$ ) and X-ray luminosity could reflect a dependence of the radio power on the cluster mass. A correlation of the type  $P_{1.4 \text{ GHz}} \propto M^{2.3}$  has been derived [66], [48], where  $M$  is the total gravitational mass within a radius of  $3h_{50}^{-1}$  Mpc. Using the cluster mass within the virial radius, the correlation is steeper (Cassano et al. in preparation). A correlation of radio power vs cluster mass could indicate that the cluster mass may be a crucial parameter in the formation of radio halos, as also suggested by [23]. Since it is likely that massive clusters are the result of several major mergers, it is concluded that both past mergers and current mergers are the necessary ingredients for the formation and evolution of radio halos. This scenario may provide a further explanation of the fact that not all clusters showing recent mergers host radio halos, which is expected from the recent modeling of Cassano & Brunetti [24].

### 3.2 Radio relics

Relic sources are diffuse extended sources, similar to the radio halos in their low surface brightness, large size ( $\gtrsim 1$  Mpc) and steep spectrum ( $\alpha \gtrsim 1$ ), but they are generally detected in the cluster peripheral regions. They typically show an elongated radio structure with the major axis roughly perpendicular

to the direction of the cluster radius, and they are strongly polarized ( $\sim 20\text{--}30\%$ ). The most extended and powerful sources of this class are detected in clusters with central radio halos: in the Coma cluster (the prototype relic source 1253+275, [56], A2163 [45], A2255 [42], A2256 [103] and A2744 (Fig. 7, left panel). A spectacular example of two giant almost symmetric relics in the same cluster is found in A3667 (Fig. 7, right panel). There are presently only a few cases of double opposite relics in clusters.

Other morphologies have been found to be associated with relics (see [61] for a review). In the cluster A1664 (Fig. 8, left panel), the structure is approximately circular and regular. In A115 (Fig. 8, right panel), the elongated relic extends from the cluster center to the periphery. This could be due to projection effects, however this is the only relic showing such behaviour.

There are diffuse radio sources which are naturally classified as relics, because of their non-central cluster location, but their characteristics are quite different from those of giant relics. Examples of these sources are in A13, A85 (Fig. 9), A133, A4038 [111]: they show a much smaller size than relics ( $\lesssim 300$  kpc down to  $\sim 50$  kpc), are generally closer to the cluster center, and show extremely steep radio spectra ( $\alpha \gtrsim 2$ ). They are strongly polarized ( $\gtrsim 30\%$ ), and often quite filamentary when observed with sufficient resolution. The relic in A133 was suggested to be related to past activity of a nearby galaxy [50].

The detection rate of radio relics in a complete sample of clusters is  $\sim 6\%$  at the detection limit of the NVSS [60]. Relics are found in clusters both with and without a cooling core, suggesting that they may be related to minor or off-axis mergers, as well as to major mergers. Theoretical models propose that they are tracers of shock waves in merger events (see § 4.3). This is consistent with their elongated structure, almost perpendicular to the merger axis. The radio power of relics correlates with the cluster X-ray luminosity ([46, 61], as also found for halos (see § 3.1 and Fig. 6), although with a larger dispersion. The existence of this correlation indicates a link between the thermal and relativistic plasma also in peripheral cluster regions.

### 3.3 Mini-halos

Mini-halos are small size ( $\sim 500$  kpc) diffuse radio sources at the center of cooling core clusters, usually surrounding a powerful radio galaxy, as in the Perseus cluster (Fig. 10, left panel), Virgo cluster [95], PKS 0745-191 [4], A2626 [63]. Since there is an anticorrelation between the presence of a cooling core and that of a major merger event, mini-halos are the only diffuse sources which are not associated with cluster mergers. A peculiar example is represented by the cluster A2142, which contains a cooling core but also shows a cold front and thus merging activity [87]. The mini-halo in this cluster is about 200 kpc in size and does not surround any powerful radio galaxy (Fig. 10, right panel). For the latter reason, it could be also considered as a small halo.

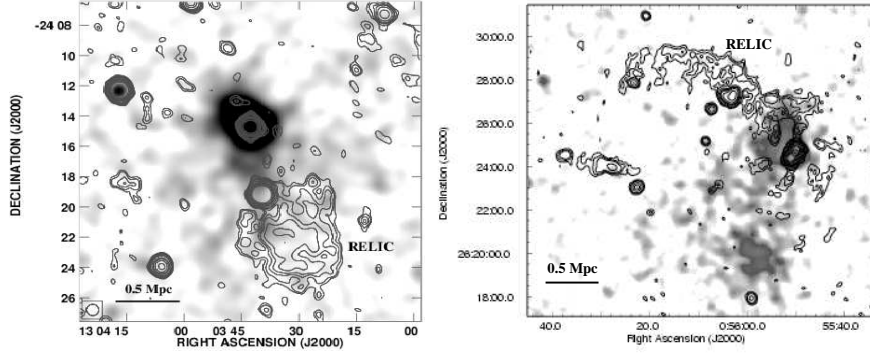


**Fig. 8.** Radio emission at 20 cm (contours) of the clusters: **Left panel:** A1664 ( $z = 0.128$ ), **Right panel:** A115 ( $z = 0.197$ ), superimposed onto the grey-scale cluster X-ray emission detected from ROSAT PSPC [66].

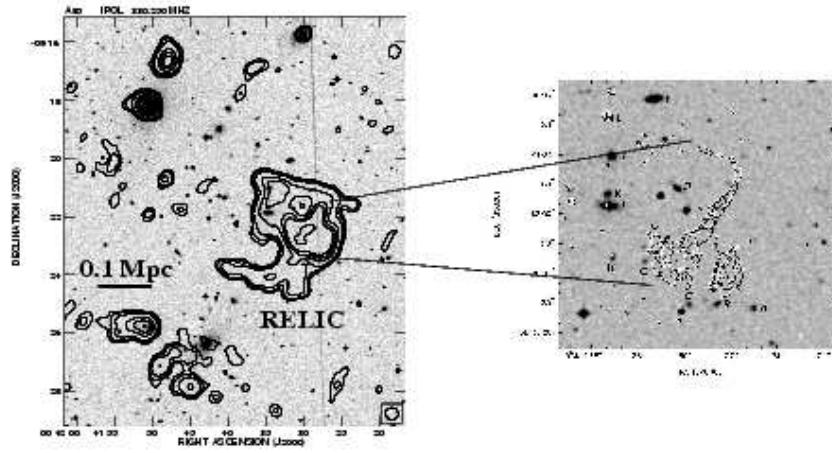


**Fig. 9.** Radio emission at 90 cm (contours) in A85 ( $z = 0.056$ ), superimposed onto the optical image [59]. The zoom to the right shows the filamentary structure detected at high resolution by Slee et al. [111] at 20 cm.

The radio spectra of mini-halos are steep, as those of halos and relics. In the Perseus mini-halo, the integrated spectrum steepens at high frequency and the spectral index distribution shows a radial steepening [110].

Gitti et al. [62] argued that the radio emitting particles in mini-halos cannot be connected to the central radio galaxy in terms of particle diffusion or buoyancy, but they are likely associated with the ICM in the cooling flow region (see § 4.4). This is supported by the correlation observed between the mini-halo radio power and the cooling flow power [63]; however, the number of objects is still low and the parameters are affected by large errors.

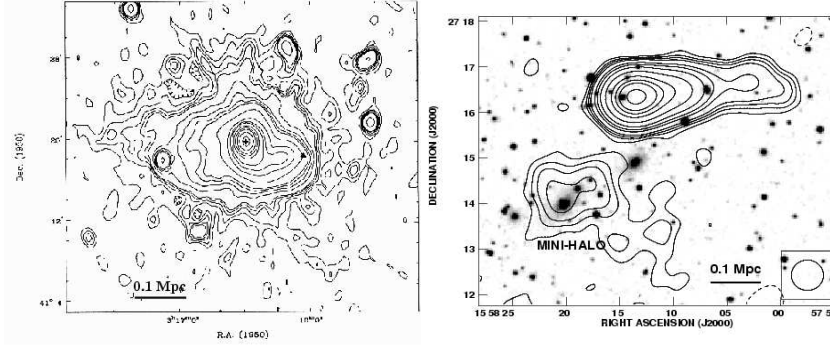


**Fig. 10.** **Left panel:** Radio contour map of the mini-halo in the Perseus cluster ( $z = 0.018$ ) at 92 cm [110], **Right panel:** The mini-halo in A2142 ( $z = 0.089$ ), superimposed onto the optical image [59].

## 4 Radio emitting particles

From the diffuse radio emission described in the previous sections, it is determined that highly energetic relativistic electrons ( $\gamma \sim 10^4$ ) are present in clusters, either in the central or in the peripheral regions. They are found both in merging (halos and relics) and relaxed (mini-halos) clusters, thus under different cluster conditions. These radio features are currently not known to be present in all clusters. They show steep radio spectra, thus the radiating particles have short lifetimes ( $\sim 10^8$  yr). Given the large size of the radio emitting regions, the relativistic particles need to be reaccelerated by some mechanism, acting with an efficiency comparable to the energy loss processes. Several possibilities have been suggested for the origin of relativistic electrons and for the mechanisms transferring energy into the relativistic electron population.

### 4.1 Connection between halos/relics and cluster merger processes

Evidence favours the hypothesis that clusters with halos and relics are characterized by strong dynamical activity, related to merging processes. These clusters indeed show: (i) substructures and distortions in the X-ray brightness distribution [109]; (ii) temperature gradients [86] and gas shocks [90]; (iii) absence of a strong cooling flow [109]; (iv) values of the spectroscopic  $\beta$  parameter which are on average larger than 1 [46]; (v) core radii significantly larger than those of clusters classified as single/primary [46]; (vi) larger distance from the nearest neighbours, compared to clusters with similar X-ray luminosity [108]. The fact that they appear more isolated supports the idea that recent merger events lead to a depletion of the nearest neighbours.

Buote [23] derived a correlation between the radio power of halos and relics and the dipole power ratio of the cluster two-dimensional gravitational

potential. Since power ratios are closely related to the dynamical state of a cluster, this correlation represents the first attempt to quantify the link between diffuse sources and cluster mergers.

Maps of the radio spectral index between 0.3 GHz and 1.4 GHz of the halos in the two clusters A665 and A2163 show that the regions influenced by the merger, as deduced from X-ray maps, show flatter spectra [49]. This is the first direct confirmation that the cluster merger supplies energy to the radio halo. Finally, we point out that we are not presently aware of any radio halo or relic in a cluster where the presence of a merger has been clearly excluded.

## 4.2 Relativistic electrons in radio halos

**Origin.** The relativistic electrons present in the cluster volume, which are responsible for the diffuse radio emission, can be either *primary* or *secondary electrons*. Primary electrons were injected into the cluster volume by AGN activity (quasars, radio galaxies, etc.), or by star formation in normal galaxies (supernovae, galactic winds, etc.) during the cluster dynamical history. This population of electrons suffers strong radiation losses mainly because of synchrotron and inverse Compton emission, thus reacceleration is needed to maintain their energy to the level necessary to produce radio emission. For this reason, primary electron models can also be referred to as reacceleration models. These models predict that the accelerated electrons have a maximum energy at  $\gamma < 10^5$  which produces a high frequency cut-off in the resulting synchrotron spectrum [20]. Thus a high frequency steepening of the integrated spectrum is expected, as well as a radial steepening and/or a complex spatial distribution of the spectral index between two frequencies, the latter due to different reacceleration processes in different cluster regions. Moreover, in these models, a tight connection between radio halos and cluster mergers is expected.

Secondary electrons are produced from inelastic nuclear collisions between the relativistic protons and the thermal ions of the ambient intracluster medium. The protons diffuse on large scales because their energy losses are negligible. They can continuously produce *in situ* electrons, distributed throughout the cluster volume [10]. Secondary electron models can reproduce the basic properties of the radio halos provided that the strength of the magnetic field, averaged over the emitting volume, is larger than a few  $\mu\text{G}$ . They predict synchrotron power-law spectra which are independent on cluster location, i.e., do not show any features and/or radial steepening, and the spectral index values are flatter than  $\alpha \sim 1.5$  [20]. The profiles of the radio emission should be steeper than those of the X-ray gas (e.g. [67]). Since the radio emitting electrons originate from protons accumulated during the cluster formation history, no correlation to recent mergers is expected, but halos should be present in virtually all clusters. Moreover, emission of gamma-rays and of neutrinos is predicted.

Present observational results, i.e., the behaviour of radio spectra (see § 3.1), the association between radio halos and cluster mergers (§ 4.1), and the fact that halos are not common in galaxy clusters [81], are in favour of electron reacceleration models. A two-phase scenario including the first phase of particle injection, followed by a second phase during which the aged electrons are reaccelerated by recent merging processes was successfully applied by Brunetti et al. [19] to the radio halo Coma C, reproducing its observational properties.

**Reacceleration.** In the framework of primary electron models, a cluster merger plays a crucial role in the energetics of radio halos. Energy can be transferred from the ICM thermal component to the non-thermal component through two possible basic mechanisms: 1) acceleration at shock waves [107, 77]; 2) resonant or non-resonant interaction of electrons with magnetohydrodynamic (MHD) turbulence [19, 21, 97, 51].

Shock acceleration is a first-order Fermi process of great importance in radio astronomy, since it is recognized as the mechanism responsible for particle acceleration in the supernova remnants. The acceleration occurs diffusively, in that particles scatter back and forth across the shock, gaining at each crossing and recrossing an amount of energy proportional to the energy itself. The acceleration efficiency is mostly determined by the shock Mach number. In the case of radio halos, however, the following arguments do not favour a connection to merger shocks: i) the shocks detected so far with Chandra at the center of several clusters (e.g. A2744, [76]; A665, [88]; 1E0657-56, [89]) have inferred Mach numbers in the range of  $\sim 1 - 2.5$ , which seem too low to accelerate the radio halo electrons [53]; ii) the radio emission of halos can be very extended up to large scales, thus it is hardly associable with localized shocks; iii) the comparison between radio data and high resolution Chandra X-ray data, performed by Govoni et al. [70], shows that some clusters exhibit a spatial correlation between the radio halo emission and the hot gas regions. This is not a general feature, however, and in some cases the hottest gas regions do not exhibit radio emission; iv) the radio spectral index distribution in A665 [49] shows no evidence of spectral flattening at the location of the hot shock detected by Chandra [88].

Although it cannot be excluded that shock acceleration may be efficient in some particular regions of a halo (e.g. in A520, [92]), current observations globally favour the scenario that cluster turbulence might be the major mechanism responsible for the supply of energy to the electrons radiating in radio halos. Numerical simulations indicate that mergers can generate strong fluid turbulence on scales of 0.1 - 1 Mpc. Turbulence acceleration is similar to a second-order Fermi process and is therefore rather inefficient compared with shock acceleration. The time during which the process is effective is only a few  $10^8$  years, so that the emission is expected to correlate with the most recent or ongoing merger event. The mechanism involves the following steps [12, 21]:



- 1) the fluid turbulence which is injected into the ICM must be converted to MHD turbulence; the mechanism for this process is not fully established (although the Lighthill mechanism is mostly used in the recent literature);
- 2) several types of MHD turbulence modes can be activated (Alfvén waves, slow and fast magnetosonic modes, etc.) and each of them has a different channel of wave-particle interaction;
- 3) the cascade process due to wave-wave interaction, i.e., the decay of the MHD scale size to smaller values, must be efficient to produce the MHD scale relevant for the wave-particle interaction, i.e., for the particle reacceleration process;
- 4) the MHD waves are damped because of wave-particle interaction, so the reacceleration process could be eventually reduced.

The particle reacceleration through Alfvén waves has the following limitations: i) the scale relevant for wave-particle interaction is  $\sim 1$  pc, thus the reacceleration process is efficient only after a significant cascade process; ii) Alfvén waves are strongly damped through interaction with protons. It follows that if protons are too abundant in the ICM, they suppress the MHD turbulence and consequently the reacceleration of electrons. Brunetti et al. [21] derived that the energy in relativistic protons should be  $< 5\text{-}10\%$  than the cluster thermal energy to generate radio halos. In the case of fast magnetosonic (MS) waves, the difficulty of wave cascade to small scales is alleviated by the fact that their scale of interaction with particles is of the order of a few kpc. Moreover, the MS wave damping is due to thermal electrons, and thus hadrons do not significantly affect the electron reacceleration process [24]. Therefore, fast MS waves represent a promising channel for the MHD turbulence reacceleration of particles.

The emerging scenario is that turbulence reacceleration is the likely mechanism to supply energy to the radio halos. All the different aspects discussed above need to be further investigated in time-dependent regimes, considering all types of charged particles [22], and the contribution of different mechanisms.

### 4.3 Relativistic electrons in radio relics

Peripheral cluster regions do not host a sufficiently dense thermal proton population which is required as the target for the efficient production of secondary electrons, and therefore secondary electron models cannot operate in the case of relics. There is increasing evidence that the radio emitting particles in relics are powered by the energy dissipated in shock waves produced in the ICM by the flows of cosmological large-scale structure formation. The production of outgoing shock waves at the cluster periphery is indeed observed in numerical simulations of cluster merger events [106]. Because of the electron short radiative lifetimes, radio emission is produced close to the location of the shock waves. This is consistent with the almost perpendicular to the merger axis elongated structure of relics. The electron acceleration required to produce

the relic emission could result from Fermi-I diffusive shock acceleration of thermal ICM electrons [33], or by adiabatic energization of relativistic electrons confined in fossil radio plasma, released by a former active radio galaxy [34, 35, 73]. These models predict that the magnetic field within the relic is aligned with the shock front, and that the radio spectrum is flatter at the shock edge, where the radio brightness is expected to decline sharply.

The detection of shocks in the cluster outskirts is presently very difficult because of the very low X-ray brightness of these regions. The X-ray data for radio relics are indeed very scarce. The Chandra data of A754 [91] indicate that the easternmost boundary of the relic coincides with a region of hotter gas. From XMM data of the same cluster, Henry et al. [72] show that the diffuse radio sources (halo + relic) appear to be associated with high pressure regions.

#### 4.4 Relativistic electrons in mini-halos

Current models for mini-halos involve primary or secondary electrons, similar to halos. Gitti et al. [62] suggest that the relativistic primary electrons are continuously undergoing reacceleration due to the MHD turbulence associated with the cooling flow region. Pfrommer & Enßlin [98], on the other hand, discuss the possibility that relativistic electrons in mini-halos are of secondary origin and thus are produced by the interaction of cosmic ray protons with the ambient thermal protons. Predictions of these models are similar to those of the halo models. The electron reacceleration model is favoured by the spectral behaviour of the Perseus mini-halo, i.e. high frequency steepening and radial spectral steepening [110], and by the observed correlation between the mini-halo radio power and the cooling flow power [62]. Data on this class of diffuse radio sources, however, are too poor to draw conclusions.

### 5 Cluster magnetic fields

The presence of magnetic fields in clusters is directly demonstrated by the existence of large-scale diffuse synchrotron sources, which have been discussed in § 3. In this section, we present an independent way of obtaining indirect information about the cluster magnetic field strength and geometry, using data at radio wavelengths. This is the analysis of the Faraday rotation of radio sources in the background of clusters or in the galaxy clusters themselves.

Measurements of the ICM magnetic fields can also be obtained through X-ray data from the studies of cold fronts (e.g. [119]) and from the detection of non-thermal X-ray emission of inverse Compton origin, due to scattering of the cosmic microwave background photons by the synchrotron electrons. The latter emission can be detected in the hard X-ray domain (e.g. [52]), where the cluster thermal emission becomes negligible. The studies in the radio band are, however, the most relevant and provide the most detailed field estimates.

### 5.1 Rotation measure

The synchrotron radiation from cosmic radio sources is well known to be linearly polarized. A linearly polarized wave of wavelength  $\lambda$ , traveling from a radio source through a magnetized medium, experiences a phase shift of the left versus right circularly polarized components of the wavefront, leading to a rotation  $\Delta\chi$  of the position angle of the polarization, according to the law:  $\Delta\chi = \text{RM} \lambda^2$ , where RM is the Faraday rotation measure. The RM is obtained as:

$$\text{RM} = \frac{e^3}{2\pi m_e^2 c^4} \int_0^L n_e \mathbf{B} \cdot d\mathbf{l}. \quad (20)$$

In practical units, RM is related to the electron density  $n_e$ , in units of  $\text{cm}^{-3}$ , and to the magnetic field along the line of sight  $B_{\parallel}$ , in units of  $\mu\text{G}$ , through the relation:

$$\text{RM} = 812 \int_0^L n_e B_{\parallel} dl \quad \text{rad m}^{-2}, \quad (21)$$

where the path length  $l$  is in kpc. By convention, RM is positive (negative) for a magnetic field directed toward (away from) the observer.

The RM values can be derived from multi-frequency polarimetric observations of sources within or behind the clusters, by measuring the position angle of the polarized radiation as a function of wavelength. In general, the position angle must be measured at three or more wavelengths in order to determine RM accurately and remove the position angle ambiguity:  $\chi_{\text{true}} = \chi_{\text{obs}} \pm n\pi$ . Once the contribution of our Galaxy is subtracted, the RM should be dominated by the contribution of the ICM, and therefore it can be combined with measurements of  $n_e$  to estimate the cluster magnetic field along the line of sight. This approach can be followed analytically only for simple distributions of  $n_e$  and  $B$ .

A recent technique to analyse and interpret the RM data is the RM Synthesis, developed by Brentjens & De Bruyn [17], which uses the RM transfer function to solve the  $n\pi$  ambiguity related to the RM computation, and allows one to distinguish the emission as a function of Faraday depth.

Below we present some simple cases, where the strength of the magnetic field can be derived by RM measurements:

**Uniform screen.** In the simplest approximation of an external screen with uniform magnetic field, no depolarization is produced and the rotation measure follows directly from eqn. (21):

$$\text{RM} = 812 n_e B_{\parallel} L, \quad (22)$$

where  $n_e$  is in  $\text{cm}^{-3}$ ,  $B_{\parallel}$  is in  $\mu\text{G}$ , and  $L$  is the depth of the screen in kpc.

**Screen with tangled magnetic field.** The effect of a Faraday screen with a tangled magnetic field has been analyzed by Lawler and Dennison [82] and by Tribble [116] in the ideal case that the screen is made of cells of uniform size, with the same electron density and the same magnetic field strength, but with field orientation at random angles in each cell. The observed RM along any given line of sight will be generated by a random walk process, which results in a gaussian RM distribution with mean and variance given by:

$$\langle \text{RM} \rangle = 0, \quad \sigma_{\text{RM}}^2 = \langle \text{RM}^2 \rangle = 812^2 \Lambda_c \int (n_e B_{\parallel})^2 dl, \quad (23)$$

where  $n_e$  is in  $\text{cm}^{-3}$ ,  $B$  is in  $\mu\text{G}$ , and  $\Lambda_c$  is the size of each cell in kpc. A tangled magnetic field also produces depolarization (see [116]).

**Screen with tangled magnetic field and radial gas density distribution.** The case of a screen with tangled magnetic field can be treated analytically if a realistic cluster gas density distribution is considered, given that the cells have uniform size, the same magnetic field strength and random field orientation. If the gas density follows a hydrostatic isothermal beta model [25], i.e.,

$$n_e(r) = n_0 (1 + r^2/r_c^2)^{-\frac{3\beta}{2}}, \quad (24)$$

where  $n_0$  is the central electron density, and  $r_c$  is the core radius of the gas distribution, the value of the RM variance is given by:

$$\sigma_{\text{RM}}(r_{\perp}) = \frac{K B n_0 r_c^{\frac{1}{2}} \Lambda_c^{\frac{1}{2}}}{(1 + r_{\perp}^2/r_c^2)^{\frac{(6\beta-1)}{4}}} \sqrt{\frac{\Gamma(3\beta - 0.5)}{\Gamma(3\beta)}}, \quad (25)$$

where  $r_{\perp}$  is the projected distance from the cluster centre and  $\Gamma$  indicates the Gamma function. The constant  $K$  depends on the integration path over the gas density distribution:  $K = 624$ , if the source lies completely beyond the cluster, and  $K = 441$  if the source is halfway through the cluster.

For  $\beta=0.7$  the previous formula becomes:

$$\sigma_{\text{RM}} \approx \frac{575 B}{(1 + r^2/r_c^2)^{0.8}} n_0 M^{\frac{1}{2}} l. \quad (26)$$

Note that depolarization is also produced, due to the fact that the magnetic field is tangled.

## 5.2 Current results from RM studies

Cluster surveys of the Faraday rotation measures of polarized radio sources both within and behind clusters provide an important probe of the existence of intracluster magnetic fields. The RM values derived in background or embedded cluster sources are of the order of tens to thousands  $\text{rad m}^{-2}$  (an example is shown in Fig. 11). The observing strategy to derive information

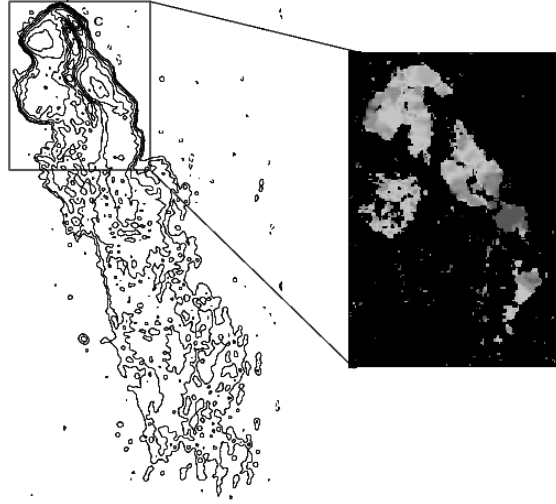


**Fig. 11.** VLA contour plot of the tailed radio galaxy 0053-015 in A119 at 1.4 GHz (left), and RM image (right). The values of RM range between  $-350 \text{ rad m}^{-2}$  and  $+450 \text{ rad m}^{-2}$ , with  $\langle \text{RM} \rangle = +28 \text{ rad m}^{-2}$ , and a dispersion of  $\sigma_{\text{RM}} = 152 \text{ rad m}^{-2}$ . They show fluctuations on scales of  $\sim 3.5 \text{ arcsec}$  [44].

on the magnetic field intensity and structure is twofold: i) obtain the average value of the RM of sources located at different impact parameters of the cluster, ii) derive maps of the RM of extended radio sources, to evaluate the  $\sigma$  of the RM distribution.

Studies have been carried out on both statistical samples and individual clusters (see e.g. the review by Govoni & Feretti [69] and references therein). Kim et al. [78] analyzed the RM of 53 radio sources in and behind clusters and 99 sources in a control sample. This study, which contains the largest cluster sample to date, demonstrated that  $\mu\text{G}$  level fields are widespread in the ICM. In a more recent statistical study, Clarke et al. [27] analyzed RMs for a representative sample of 16 cluster sources, plus a control sample, and found a statistically significant broadening of the RM distribution in the cluster sample, and a clear increase in the width of the RM distribution toward smaller impact parameters (see Fig. 12). They derived that the ICM is permeated with a high filling factor of magnetic fields at levels of  $4 - 8 \mu\text{G}$  and with a correlation length of  $\sim 15 \text{ kpc}$ , up to  $\sim 0.75 \text{ Mpc}$  from the cluster centre. The results are confirmed by new data on an expanded sample [28].

The first detailed studies of RM within individual clusters have been performed on cooling core clusters, owing to the extremely high RMs of the powerful radio galaxies at their centres (e.g., Hydra A, [113]; 3C295, [1]). High values of the magnetic fields, up to tens of  $\mu\text{G}$ , have been obtained, but they only refer to the innermost cluster regions. Studies on larger areas of clusters have been carried out e.g. for Coma [41], A119 [44], A514 [68], 3C129 [114].

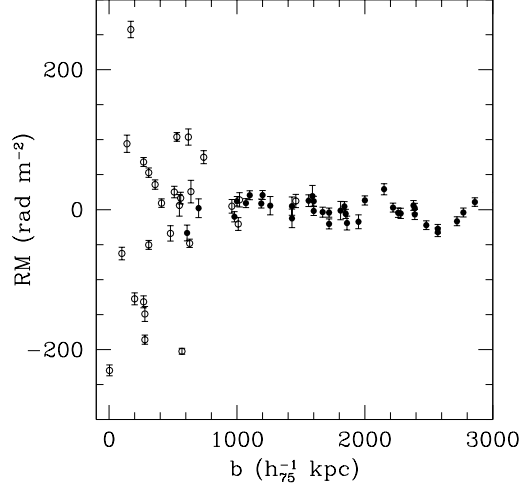


**Fig. 12.** Galaxy-corrected rotation measure plotted as a function of source impact parameter in kiloparsecs for the sample of sources from Clarke et al. [27]. Open dots refer to cluster sources, closed dots to control sources.

Overall, the data are consistent with cluster atmospheres containing magnetic fields in the range of  $1\text{--}5\ \mu\text{G}$ , regardless of the presence or not of diffuse radio emission. At the centre of cooling core clusters, magnetic field strengths can be larger by more than a factor of 2. The RM distributions are generally patchy, indicating that large-scale magnetic fields are not regularly ordered on cluster scales, but have coherence scales between 1 and 10 kpc. In most clusters the magnetic fields are not dynamically important, with magnetic pressures much lower than the thermal pressures, but the fields may play a fundamental role in the suppression of the particle thermal conduction [26] and in the energy budget of the ICM.

### 5.3 Magnetic field structure

The simplest model is a uniform field throughout the cluster. However, this is not realistic: if the field values detected at the cluster centres extend over several core radii, up to distances of the order of  $\sim \text{Mpc}$ , then the magnetic pressure would exceed the thermal pressure in the outer parts of the clusters. The magnetic field intensity is likely to decrease with the distance from the cluster centre, as derived in Coma [19]. This is also predicted as a result of compression of the thermal plasma during the cluster gravitational collapse, where the magnetic field-lines are frozen into the plasma, and compression of the plasma results in compression of flux lines. As a consequence of magnetic flux conservation, the expected growth of the magnetic field is proportional to the gas density as  $B \propto \rho^{2/3}$ .

Dolag et al. [31] showed that in the framework of hierarchical cluster formation, the correlation between two observable parameters, the RM and the X-ray surface brightness, is expected to reflect the correlation between the magnetic field and gas density. Therefore, from the analysis of the RM versus X-ray brightness it is possible to infer the trend of magnetic field versus gas density. The application of this approach has been possible so far only in A119, giving the radial profile of the magnetic field as  $B \propto n_e^{0.9}$  [31]. The magnetic field decline with radius is confirmed in this case.

Another important aspect to consider is the structure in the cluster magnetic field, i.e. the existence of filaments and flux ropes [32]. The magnetic field structure can be investigated by deriving the power spectrum of the field fluctuations, defined as:  $|B_\kappa|^2 \propto \kappa^{-n}$ , where  $\kappa$  represents the wave number of the fluctuation scale. By using a semi-analytic technique, Enßlin & Vogt [36] and Vogt & Enßlin [120] showed that the magnetic field power spectrum can be estimated by Fourier transforming RM maps, if very detailed RM images are available. Alternatively, a numerical approach using Monte Carlo simulations has been developed by Murgia et al. [94] to reproduce the rotation measure and the depolarization produced by magnetic field with different power spectra.

#### 5.4 Reconciling values derived with different approaches

The cluster magnetic field values obtained from RM arguments are about an order of magnitude higher than those derived from both the synchrotron diffuse radio emission (§ 3.1) and the inverse Compton (IC) hard X-ray emission (e.g. [52]). The discrepancy can be alleviated by taking into account that:

- estimates of equipartition fields rely on several assumptions (see § 2.3);
- Goldsmith & Rephaeli [64] suggested that the IC estimate is typically expected to be lower than the Faraday rotation estimate, because of the spatial profiles of the magnetic field and gas density. For example, if the magnetic field strength has a radial decrease, most of the IC emission will come from the weak field regions in the outer parts of the cluster, while most of the Faraday rotation and synchrotron emission occurs in the strong field regions in the inner parts of the cluster;
- it has been shown that IC models which include the effects of aged electron spectra, combined with the expected radial profile of the magnetic field, and anisotropies in the pitch angle distribution of the electrons, allow higher values of the ICM magnetic field in better agreement with the Faraday rotation measurements [19, 97];
- the magnetic field may show complex structure, as filamentation and/or substructure with a range of coherence scales (power spectrum). Therefore, the RM data should be interpreted using realistic models of the cluster magnetic fields (see § 5.3);

- Beck et al. [5] pointed out that field estimates derived from RM may be too large in the case of a turbulent medium where small-scale fluctuations in the magnetic field and the electron density are highly correlated ;
- it has been recently pointed out that in some cases a radio source could compress the gas and fields in the ICM to produce local RM enhancements, thus leading to overestimates of the derived ICM magnetic field strength [105];
- evidence suggests that the magnetic field strength will vary depending on the dynamical history and location within the cluster. A striking example of the variation of magnetic field strength estimates for various methods and in various locations throughout the cluster is given in [74].

Future studies are needed to shed light on these issues and improve our current knowledge on the strength and structure of the magnetic fields.

### 5.5 Origin of cluster magnetic fields

The field strengths that we observe in clusters greatly exceed the amplitude of the seed fields produced in the early universe, or fields injected by some mechanism by high redshift objects. There are two basic possibilities for their origin:

- 1) ejection from galactic winds of normal galaxies or from active and starburst galaxies [80, 121];
- 2) amplification of seed fields during the cluster formation process.

Support for a galactic injection in the ICM comes from the evidence that a large fraction of the ICM is of galactic origin, since it contains a significant concentration of metals. However, fields in clusters have strengths and coherence size comparable to, and in some cases larger than, galactic fields [71]. Therefore, it seems quite difficult that the magnetic fields in the ICM derive purely from ejection of the galactic fields, without invoking other amplification mechanisms [29, 101].

Magnetic field amplification is likely to occur during the cluster collapse, simply by compression of an intergalactic field. Clusters have present day overdensities  $\rho \sim 10^3$  and in order to get  $B_{\text{ICM}} > 10^{-6}$  G by adiabatic compression ( $B \propto \rho^{2/3}$ ) requires intergalactic (seed) fields of at least  $10^{-8}$  G. These are somewhat higher than current limits derived in the literature [3, 11]. A possible way to obtain a larger field amplification is through cluster mergers. Mergers generate shocks, bulk flows and turbulence within the ICM. The first two of these processes can result in some field amplification simply through compression. However, it is the turbulence which is the most promising source of non-linear amplification. MHD calculations have been performed [30, 102, 112] to investigate the evolution of magnetic fields. The results of these simulations show that cluster mergers can dramatically alter the local strength and structure of cluster-wide magnetic fields, with a strong amplification of the magnetic field intensity. Shear flows are extremely important



for the amplification of the magnetic field, while the compression of the gas is of minor importance. The initial field distribution at the beginning of the simulations at high redshift is irrelevant for the final structure of the magnetic field. The final structure is dominated only by the cluster collapse. Fields can be amplified from initial values of  $\sim 10^{-9}$  G at  $z = 15$  to  $\sim 10^{-6}$  G at the present epoch [30]. Roettiger et al. [102] found a significant evolution of the structure and strength of the magnetic fields during two distinct epochs of the merger evolution. In the first, the field becomes quite filamentary as a result of stretching and compression caused by shocks and bulk flows during infall, but only minimal amplification occurs. In the second, amplification of the field occurs more rapidly, particularly in localized regions, as the bulk flow is replaced by turbulent motions. Mergers change the local magnetic field strength drastically, but also the structure of the cluster-wide field is influenced. At early stages of the merger the filamentary structures prevail. This structure breaks down later ( $\sim 2\text{--}3$  Gyr) and leaves a stochastically ordered magnetic field. Subramanian et al [112] argue that the dynamo action of turbulent motions in the intracluster gas can amplify a random magnetic field by a net factor of  $10^4$  in 5 Gyr. The field is amplified by random shear, and has an intermittent spatial distribution, possibly producing filaments.

## 6 Radio emission from cluster radio galaxies

Recent results on the thermal gas in clusters of galaxies has revealed a significant amount of spatial and temperature structure, indicating that clusters are dynamically evolving by accreting gas and galaxies and by merging with other clusters/groups (roughly every few Gyrs). Simulations suggest that the ICM within clusters is violent, filled with shocks, high winds and turbulence. This gas can interact with a radio source in different ways: modifying its morphology via ram pressure, confining the radio lobes, possibly feeding the active nucleus. We discuss below some of the recent results on these topics (see also the review of Feretti & Venturi [47]).

### 6.1 Interaction between the radio galaxies and the ICM

**Tailed radio galaxies.** A dramatic example of the interaction of the radio galaxies with the ICM is represented by the tailed radio galaxies, i.e. low-power radio sources (FR I type, [38]) where the large scale low-brightness emission is bent towards the same direction, forming features similar to tails. These radio galaxies were originally distinguished in two classes: narrow-angle tailed sources (NAT), which are "U" shaped with a small angle between the tails, and wide-angle tailed sources (WAT), which are "V" shaped with a larger angle between the tails (see Fig. 13). We note that distortions in powerful radio galaxies (FR II type, [38]) are marginal and only present in weak structures.

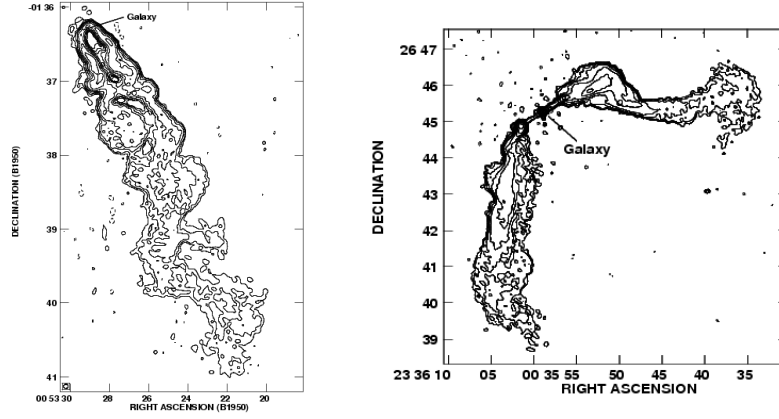


**Fig. 13.** Examples of tailed radio galaxies: the NAT 0053-016 in the cluster A119 (**left panel**) and the WAT 3C465 in the cluster A2634 (**right panel**). The location of the optical galaxy is indicated.

The standard interpretation of the tailed radio morphology is that the jets are curved by ram pressure from the high-velocity host galaxy moving through the dense ICM, whereas the low brightness tails are material left behind by the galaxy motion. The ram-pressure model was first developed by Begelman et al. [7]. Following dynamical arguments, the bending is described by the Euler equation:

$$R \sim h \left( \frac{\rho_j}{\rho_e} \right) \left( \frac{v_j}{v_g} \right)^2, \quad (27)$$

where  $R$  is the radius of curvature,  $\rho$  is density,  $v$  is velocity (the subscript  $j$  refers to the jet,  $e$  to the external medium,  $g$  to the galaxy) and  $h$  is the scale height over which the ram pressure is transmitted to the jets. Thus, from the jet bending, important constraints on both the jet dynamics and the ICM can be placed. In some cases there is evidence that the radio jets travel first through the galactic atmosphere and then are sharply bent at the transition between the galactic atmosphere and the ICM. Bends can occur very close to the nucleus, as in NGC 4869 in the Coma cluster [40], indicating that the bulk of interstellar medium has been stripped by the galaxy during its motion.

In general, the ram-pressure model can explain the radio jet deflection when the galaxy velocity with respect to the ICM is of the order of  $\sim 1000 \text{ km s}^{-1}$ . Therefore, it can successfully explain the structure of NAT sources, which are indeed identified with cluster galaxies located at any distance from the cluster centre and thus characterized by significant motion. However, Bliton et al. [13] derived that NATs are preferentially found in clusters with X-ray substructure. Additionally, NAT galaxies tend to have, on average, velocities

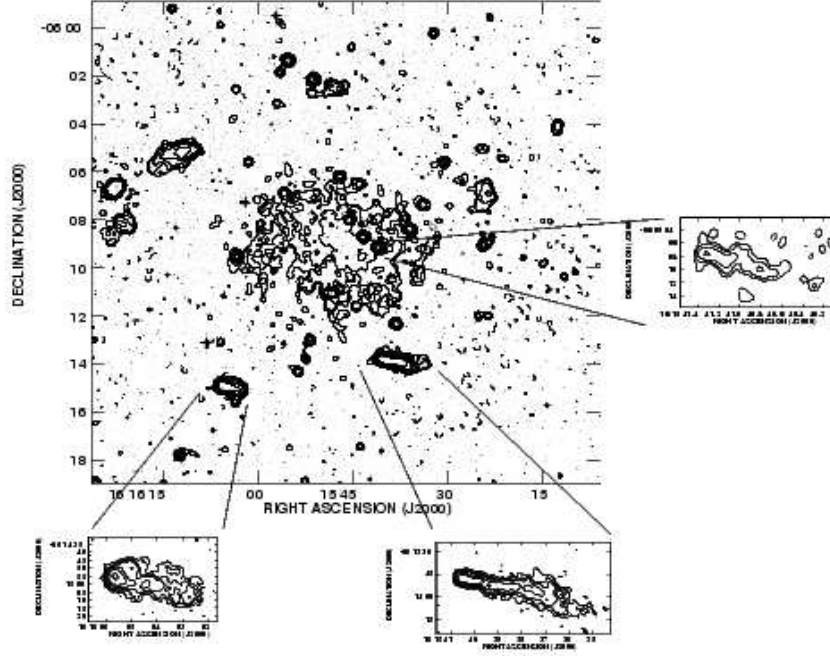


**Fig. 14.** Radio image of the cluster A2163 at 1.4 GHz, with angular resolution of  $15''$  [45]. The structure of tailed radio galaxies as detected at higher resolution is shown in the insets. The tails are all oriented in the same direction.

similar to those of typical cluster members, instead of high peculiar motions expected if NATs were bent only from ram pressure. Thus, they suggested a new model for the NAT formation, in which NATs are associated with dynamically complex clusters with possible recent or ongoing cluster-subcluster mergers. The U-shaped morphology is then suggested to be produced, at least in part, by the merger-induced bulk motion of the ICM bending the jets. This is supported, in some clusters, by the existence of NAT radio galaxies with their tails oriented in the same direction (e.g., A2163, Fig. 14; A119, [44]), since it seems unlikely that their parent galaxies are all moving towards the same direction.

The interpretation of WAT sources may be problematic in the framework of the ram-pressure model, since these sources are generally associated with dominant cluster galaxies moving very slowly ( $\lesssim 100 \text{ km s}^{-1}$ ) relative to the cluster velocity centroid. Such slow motion is insufficient to bend the jets/tails of WATs to their observed curvature by ram pressure. It has therefore been suggested that WATs must be shaped mostly by other ram-pressure gradients not arising from the motion of the host galaxy, but produced by mergers between clusters [85, 65]. Numerical simulations lead support to this idea:

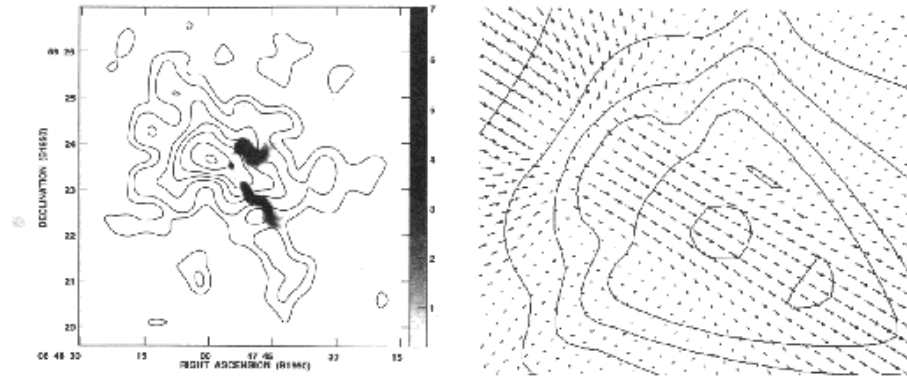


**Fig. 15.** **Left panel:** Overlay of the grey-scale radio image of the WAT source in A562 onto the ROSAT X-ray surface brightness contour image of the same cluster. **Right panel:** Overlay of a synthetic X-ray image of a cluster merger onto a velocity vector field that represents the gas velocity. Note that the X-ray contours in the left panel look very similar to the synthetic X-ray image and that the radio tails are in the direction of the gas velocity (from [65]).

peak gas velocities are found well in excess of  $1000 \text{ km s}^{-1}$  at various stages of the cluster merger evolution, which generally do not decay below  $1000 \text{ km s}^{-1}$  for nearly 2 Gyr after the core passage. This is consistent with the observations, as modelled in the cluster A562 (Fig. 15).

**Radio emission in X-ray cavities.** A clear example of the interaction between the radio plasma and the hot intracluster medium was found in the ROSAT image of the Perseus cluster [15], where X-ray cavities associated with the inner radio lobes to the north and south of the bright central radio galaxy 3C84 have been first detected. The high spatial resolution of the Chandra X-ray Observatory has confirmed the presence of such X-ray holes [37], coinciding with the radio lobes and showing rims cooler than the surrounding gas. Chandra has permitted the detection of X-ray deficient bubbles in the inner region of many cooling flow clusters, e.g., Hydra A, A2052, A496, A2199, RBS797. These features are discussed by C. Jones et al. in this volume.

## 6.2 Trigger of radio emission

An important issue is to understand whether and how the cluster environment plays any role in the statistical radio properties of galaxies, in particular their probability of forming radio sources. The high density of galaxies within clusters, especially in the innermost cluster regions, and the peculiar velocities of galaxies, most extreme in merging clusters, enhance the probability of galaxy-galaxy interactions. These special conditions raise the questions whether cluster galaxies have enhanced probability of developing a radio

source, and whether they tend to have more powerful and long lived radio emission.

A powerful statistical tool to address the above questions is the radio luminosity function (hereinafter RLF). The fractional RLF is defined as:

$$f_i(P, z) = \frac{\rho_i(P, z)}{\phi_i(z)}, \quad (28)$$

where  $\phi_i(z)$  is the density of objects of a particular class  $i$  at the epoch  $z$ , and  $\rho_i(P, z)$  is the density of the same class objects showing a radio emission of power  $P$ . The fractional RLF,  $f(P)$ , thus represents the probability that a galaxy in a defined sample at a given epoch emits with radio power in the interval  $P \pm dP$ . From an operational point of view, the RLF can be expressed as:

$$f(P) = \frac{n(\Delta P_i)}{N(\Delta P_i)}, \quad (29)$$

where  $n$  and  $N$  are respectively the number of detected radio galaxies in the power interval  $\Delta P_i$  and the total number of optical galaxies which could have been detected in the same power bin. The integral form of the RLF  $F(> P)$  can be obtained simply summing over all radio power intervals up to the power  $P$ . In order to take into account the correlation between the optical and radio properties of galaxies, it is useful to introduce the bivariate luminosity function  $f(P, M)$ , which gives the probability that a galaxy with absolute magnitude in the range  $M \pm dM$  is radio emitting in the radio power range  $P \pm dP$ .

The RLF of galaxies in clusters has been first investigated by Fanti [39], and latter by Ledlow and Owen [83]. The most striking result is that statistical properties of radio galaxies are surprisingly similar for sources both inside and outside rich clusters. For both cluster and non-cluster galaxies, the only parameter relevant for the radio emission seems to be the optical magnitude, i.e. brighter galaxies have a higher probability of developing a radio galaxy. Furthermore, the radio luminosity function is independent on richness class, Bautz-Morgan or Rood-Sastry cluster class. Recently, Best et al. [9] demonstrated that, while the radio power of a radio galaxy does not correlate to its mass, the probability of a galaxy to become a radio source is a very strong function of both stellar mass and central black hole mass.

It is still under debate whether the universality of the local RLF for early type galaxies can be applied also to merging clusters. According to some authors (e.g. [118, 54]) the enhanced probability of galaxy interaction in merging clusters has no effect on the probability of galaxies to develop a radio active galactic nucleus in their centres.

In the cluster A2255, instead, Miller & Owen [93] found an excess of powerful radio galaxies, which is interpreted as due to the dynamical state of the cluster. Best [8] showed that the fraction of radio loud AGN appears to be

strongly dependent upon the large scale environment of a galaxy. This supports the argument that a merger process may affect the AGN activity, since infalling galaxies or galaxy groups more likely produce galaxy interactions or galaxy-galaxy mergers which can trigger the AGN activity. The effect of cluster merger processes on the trigger of radio emission would imply an enhanced number of radio source in cluster at high redshift, i.e. at the earlier epochs when the clusters are being assembled. These issues are under investigation. The result of Branchesi et al. [16] points to a higher number of radio galaxies in distant clusters, although with poor statistics. In conclusion, whereas the ICM in clusters has strong effect on the structures of radio galaxies, the probability of forming radio sources is likely unaffected by the cluster environment, but may be affected by cluster mergers.

Other effects of the interaction between galaxies and ICM, as the trigger of star formation, the gas stripping, HI deficiency, etc., are discussed by other authors in this volume.

## Acknowledgements

LF is grateful to the organizers David Hughes, Omar López-Cruz and Manolis Plionis for their invitation to this stimulating and very interesting school. We acknowledge Gianfranco Brunetti for illuminating discussions on the models of relativistic particle origin and re-acceleration.

## References

1. S.W. Allen, G.B. Taylor, P.E.J. Nulsen, et al., *MNRAS*, **324**, 842 (2001)
2. M. Bacchi, L. Feretti, G. Giovannini, F. Govoni, *A&A* **400**, 465 (2003)
3. J. D. Barrow, P.G. Ferreira, J. Silk, *Phys. Rev. Lett.* **78**, 3610 (1997)
4. S.A. Baum, C.P. O’Dea, *MNRAS*, **250**, 737 (1991)
5. R. Beck, A. Sukurov, D. Sokoloff, R. Wielebinski, *A&A*, **411**, 99 (2003)
6. R. Beck, M. Krause, *Astron. Nachr.* **326**, 414 (2005)
7. M.C. Begelman, M.J. Rees, R.D. Blandford, *Nature* **279**, 770 (1979)
8. P.N. Best, *MNRAS*, **351**, 70 (2004)
9. P.N. Best, G. Kauffman, T.M. Heckman, et al., *MNRAS*, **362**, 25 (2005)
10. P. Blasi, S. Colafrancesco, *Astrop. Phys.* **12**, 169 (1999)
11. P. Blasi, S. Burles, A.V. Olinto, *ApJ* **514**, L79 (1999)
12. P. Blasi, *Proc. Int. Conf. on Cosmic Rays and Magnetic Fields in Large Scale Structure*, eds. H. Kang & D. Ryu, *Jour. Kor. Astr. Soc.* **37**, 483 (2004)
13. M. Bliton, E. Rizza, J.O. Burns, F.N. Owen, M.J. Ledlow, *MNRAS*, **301**, 609 (1998)
14. G. R. Blumenthal, R. J. Gould, *Reviews of Modern Physics* **42**, 237 (1970)
15. H. Böhringer, W. Voges, A.C. Fabian, A.C. Edge, D.M. Neumann, *MNRAS*, **264**, L25 (1993)
16. M. Branchesi, I.M. Gioia, C. Fanti, R. Fanti, R. Perley, *A&A*, **446**, 97 (2006)

17. M.A. Brentjens, A.G. de Bruyn, A&A, **441**, 1217 (2005)
18. G. Brunetti, G. Setti, A. Comastri, A&A, **325**, 898 (1997)
19. G. Brunetti, G. Setti, L. Feretti, G. Giovannini, MNRAS, **320**, 365 (2001)
20. G. Brunetti G., Proc. Int. Conf. on Cosmic Rays and Magnetic Fields in Large Scale Structure, eds. H. Kang & D. Ryu, Jour. Kor. Astr. Soc. **37**, 493 (2004)
21. G. Brunetti, P. Blasi, R. Cassano, S. Gabici, MNRAS **350**, 1174 (2004)
22. G. Brunetti, P. Blasi, MNRAS, **363**, 1173 (2005)
23. D.A. Buote, ApJ, **553**, L15 (2001)
24. R. Cassano, G. Brunetti, MNRAS, **357**, 1313 (2005)
25. A. Cavaliere, R. Fusco-Femiano, A&A, **100**, 194 (1981)
26. B.D.G. Chandran, S.C. Cowley, M. Ivanushkina, R. Sydora, ApJ, **525**, 638 (1999)
27. T.E. Clarke, P.P. Kronberg, H. Böhringer, ApJ, **547**, L111 (2001)
28. T.E. Clarke, Proc. Int. Conf. on Cosmic Rays and Magnetic Fields in Large Scale Structure, eds. H. Kang & D. Ryu, Jour. Kor. Astr. Soc. **37**, 337 (2004)
29. D.S. De Young, ApJ, **386**, 464 (1992)
30. K. Dolag, M. Bartelmann, H. Lesch, A&A, **348**, 351 (1999)
31. K. Dolag, S. Schindler, F. Govoni, L. Feretti, A&A, **378**, 777 (2001)
32. J. Eilek, In: *Diffuse thermal and relativistic plasma in galaxy clusters*, eds. H. Böhringer, L. Feretti & P. Schuecker, MPE Report **271**, p. 71 (1999)
33. T. A. Enßlin, P. L. Biermann, U. Klein, S. Kohle, A&A, **332**, 395 (1998)
34. T. A. Enßlin, Gopal-Krishna, A&A, **366**, 26 (2001)
35. T. A. Enßlin, M. Brüggen, MNRAS, **331**, 1011 (2002)
36. T. A. Enßlin, C. Vogt, A&A, **401**, 835 (2003)
37. A.C. Fabian, J.S. Sanders, S. Ettori, MNRAS **318**, L65 (2000)
38. B.L. Fanaroff, J.M. Riley, MNRAS, **167**, 31P (1974)
39. R. Fanti, In: *Clusters and Groups of Galaxies*, eds. F. Mardirossian, G. Giuricin & M. Mezzetti, Publ. Reidel, Dordrecht, p. 185 (1984)
40. L. Feretti, D. Dallacasa, G. Giovannini, T. Venturi, A&A, **232**, 337 (1990)
41. L. Feretti, D. Dallacasa, G. Giovannini, A. Tagliani, A&A, **302**, 680 (1995)
42. L. Feretti, H. Böhringer, G. Giovannini, D. Neumann, A&A, **317**, 432 (1997a)
43. L. Feretti, G. Giovannini, H. Böhringer, New Astron. **2**, 501 (1997b)
44. L. Feretti, D. Dallacasa, F. Govoni, G. Giovannini, G.B. Taylor, U. Klein, A&A, **344**, 472 (1999)
45. L. Feretti, R. Fusco-Femiano, G. Giovannini, F. Govoni, A&A, **373**, 106 (2001)
46. L. Feretti, In: *The Universe at low radio frequencies*, IAU Symp. 199, eds. Pramesh Rao, G. Swarup & Gopal-Krishna (San Francisco: ASP), p. 133 (2002)
47. L. Feretti, T. Venturi, In: *Merging Processes of Galaxy Clusters*, eds. L. Feretti, I.M. Gioia & G. Giovannini, ASSL, Kluwer Ac. Publish., p. 163 (2002)
48. L. Feretti, In: *Matter and energy in clusters of galaxies*, eds. S. Bowyer & C.-Y. Hwang, ASP Conference Series Vol. 301, p. 143 (2003)
49. L. Feretti, E. Orrú, G. Brunetti, G. Giovannini, N. Kassim, G. Setti, A&A, **423**, 111 (2004)
50. Y. Fujita, C.L. Sarazin, J.C. Kempner, et al., ApJ, **575**, 764 (2002)
51. Y. Fujita, M. Takizawa, C.L. Sarazin, ApJ, **584**, 190 (2003)
52. R. Fusco-Femiano, D. Dal Fiume, M. Orlandini, et al. In: *Matter and Energy in Clusters of Galaxies*, Eds. S. Bowyer & C.Y. Hwang, ASP Conference Series Vol. 301, p. 109, (2003)
53. S. Gabici, P. Blasi, ApJ, **583**, 695 (2003)

54. S. Giacintucci, T. Venturi, S. Bardelli, D. Dallacasa, E. Zucca, *A&A*, **419**, 71 (2004)
55. S. Giacintucci, T. Venturi, G. Brunetti, et al., *A&A*, **440**, 867 (2005)
56. G. Giovannini, L. Feretti, C. Stanghellini, *A&A* **252**, 528 (1991)
57. G. Giovannini, L. Feretti, T. Venturi, K.-T. Kim, P.P. Kronberg, *ApJ*, **406**, 399 (1993)
58. G. Giovannini, M. Tordi, L. Feretti, *New Astron.* **4**, 141 (1999)
59. G. Giovannini, L. Feretti, *New Astron.* **5**, 335 (2000)
60. G. Giovannini, L. Feretti, in *Merging Processes of Galaxy Clusters*, eds. L. Feretti, I.M. Gioia & G. Giovannini, ASSL, Kluwer Ac. Publish., p. 197 (2002)
61. G. Giovannini, L. Feretti, *Proc. Int. Conf. on Cosmic Rays and Magnetic Fields in Large Scale Structure*, eds. H. Kang & D. Ryu, *Jour. Kor. Astr. Soc.* **37**, 323 (2004)
62. M. Gitti, G. Brunetti, G. Setti, *A&A*, **386**, 456 (2002)
63. M. Gitti, G. Brunetti, L. Feretti, G. Setti, *A&A*, **417**, 1 (2004)
64. O. Goldshmidt, Y. Rephaeli, *ApJ*, **411**, 518 (1993)
65. P.L. Gómez, J. Pinkney, J.O. Burns, et al., *ApJ*, **474**, 580 (1997)
66. F. Govoni, L. Feretti, G. Giovannini, H. Böhringer, T.H. Reiprich, M. Murgia, *A&A*, **376**, 803 (2001a)
67. F. Govoni, T. Ensslin, L. Feretti, G. Giovannini, *A&A* **369**, 441 (2001b)
68. F. Govoni, G.B. Taylor, D. Dallacasa, L. Feretti, G. Giovannini, *A&A*, **379**, 807 (2001c)
69. F. Govoni, L. Feretti, *Int. J. Mod. Phys. D*, Vol. **13**, N. 8, p. 1549 (2004)
70. F. Govoni, M. Markevitch, A. Vikhlinin, L. VanSpeybroeck, L. Feretti, G. Giovannini, *ApJ*, **605**, 695 (2004)
71. D. Grasso, H.R. Rubinstein, *Physics Report* **348**, 163 (2001)
72. P.J. Henry, A. Finoguenov, U.G. Briel, *ApJ*, **615**, 181 (2004)
73. M. Hoeft, M. Brüggen, G. Yepes, *MNRAS*, **347**, 389 (2004)
74. M. Johnston-Hollitt, In: *The Riddle of Cooling Flows in Galaxies and Clusters of Galaxies*, eds. T. Reiprich, J. Kempner, & N. Soker, published electronically at <http://www.astro.virginia.edu/coolflow/> (2004)
75. N.S. Kardashev, *Soviet Astron.* **6**, 317 (1962)
76. J.C. Kempner, L.P. David, *MNRAS*, **349**, 385 (2004)
77. U. Keshet, E. Waxman, A. Loeb, *ApJ*, **617**, 281 (2004)
78. K.T. Kim, P.C. Tribble, P.P. Kronberg, *ApJ*, **379**, 80 (1991)
79. S.S. Komissarov, A.G. Gubanov, *A&A*, **285**, 27 (1994)
80. P. P. Kronberg, H. Lesch, U. Hopp, *ApJ*, **511**, 56 (1999)
81. P.-H. Kuo, C.-Y. Hwang, W.-H. Ip, *ApJ*, **604**, 108 (2004)
82. J. M. Lawler, B. Dennison, *ApJ*, **252**, 81 (1982)
83. M.J. Ledlow, F.N. Owen, *AJ*, **112**, 9 (1996)
84. H. Liang, R.W. Hunstead, M. Birkinshaw, P. Andreani, *ApJ*, **544**, 686 (2000)
85. C. Loken, K. Roettiger, J.O. Burns, M. Norman, *ApJ*, **445**, 80 (1995)
86. M. Markevitch, W.R. Forman, C.L. Sarazin, A. Vikhlinin, *ApJ*, **503**, 77 (1998)
87. M. Markevitch, T.J. Ponman, P.E.J. Nulsen, et al., *ApJ*, **541**, 542 (2000)
88. M. Markevitch, A. Vikhlinin, *ApJ*, **563**, 95 (2001)
89. M. Markevitch, A.H. Gonzalez, L. David, et al., *ApJ*, **567**, L27 (2002)
90. M. Markevitch, A. Vikhlinin, W.R. Forman, In: *Matter and energy in clusters of galaxies*, eds. S. Bowyer & C.-Y. Hwang, ASP Conference Series Vol. 301, p. 37 (2003a)



91. M. Markevitch, P. Mazzotta, A. Vikhlinin, ApJ, **586**, L19 (2003b)
92. M. Markevitch, F. Govoni, G. Brunetti, D. Jerius, ApJ, **627**, 733 (2005)
93. N.A. Miller, F.N. Owen, AJ, **125**, 2427 (2003)
94. M. Murgia, F. Govoni, L. Feretti, et al., A&A **424**, 429 (2004)
95. F.N. Owen, J.A. Eilek, N.E. Kassim, ApJ, **543**, 611 (2000)
96. A.G. Pacholczyk, *Radio Astrophysics*, San Francisco:Freeman (1970)
97. V. Petrosian, ApJ, **557**, 560 (2001)
98. C. Pfrommer, T.A. Enßlin, A&A, **413**, 17 (2004)
99. A.D. Reid, R.W. Hunstead, L. Lemonon, M.M. Pierre, MNRAS, **302**, 571 (1999)
100. T.H. Reiprich, H. Böhringer, ApJ, **567**, 716 (2002)
101. Y. Rephaeli, Comm. Mod. Phys., vol. **12**, part C, 265 (1988)
102. K. Roettiger, J.M. Stone, J.O. Burns, ApJ, **518**, 594 (1999)
103. H. Röttgering, I. Snellen, G. Miley, et al., ApJ, **436**, 654 (1994)
104. H.J.A. Röttgering, M.H. Wieringa, R.W. Hunstead, R.D. Ekers, MNRAS, **290**, 577 (1997)
105. L. Rudnick, K.M. Blundell, ApJ, **588**, 143 (2003)
106. D. Ryu, H. Kang, E. Hallman, T.W. Jones, ApJ, **593**, 599 (2003)
107. C.L. Sarazin, ApJ, **520**, 529 (1999)
108. P. Schuecker, H. Böhringer, In: *Diffuse thermal and relativistic plasma in galaxy clusters*, eds. H. Böhringer, L. Feretti & P. Schuecker, MPE Report 271, p. 43 (1999)
109. P. Schuecker, H. Böhringer, T.H. Reiprich, L. Feretti, A&A, **378**, 408 (2001)
110. L.G. Sijbring, 1993, PhD Thesis, University of Groningen,
111. O.B. Slee, A.L. Roy, M. Murgia, H. Andernach, M. Ehle, AJ, **122**, 1172 (2001)
112. K. Subramanian, A. Shukurov, N.E.L. Haugen, MNRAS, **366**, 1437 (2006)
113. G.B. Taylor, R.A. Perley, ApJ, **416**, 554 (1993)
114. G.B. Taylor, F. Govoni, S.A. Allen, A.C. Fabian, MNRAS, **326**, 2 (2001)
115. M. Thierbach, U. Klein, R. Wielebinski, A&A, **397**, 53 (2003)
116. P.C. Tribble, MNRAS, **250**, 726 (1991)
117. H. Van der Laan, G.C. Perola, A&A, **3**, 468 (1969)
118. T. Venturi, S. Bardelli, G. Zambelli, R. Morganti, R.W. Hunstead, MNRAS, **324**, 1131 (2001)
119. A. Vikhlinin, M. Markevitch, S. Murray, ApJ, **551**, 160 (2001)
120. C. Vogt, T. A. Enßlin, A&A, **412**, 373 (2003)
121. H. J. Völk, A. M. Atoyan, Astrop. Phys. **11**, 73 (1999)
122. M.A.G. Willson, MNRAS, **151**, 1 (1970)